Broadband impedance boundary conditions for the simulation of sound propagation in the time domain

Jonghoon Bin[a] and M. Yousuff Hussaini[b]
Department of Mathematics, Florida State University, Tallahassee, Florida 32306

Soogab Lee[c]
School of Mechanical and Aerospace Engineering, Seoul National University, Seoul 151-742, South Korea

(Received 4 March 2008; revised 17 July 2008; accepted 19 September 2008)

An accurate and practical surface impedance boundary condition in the time domain has been developed for application to broadband-frequency simulation in aeroacoustic problems. To show the capability of this method, two kinds of numerical simulations are performed and compared with the analytical/experimental results: one is acoustic wave reflection by a monopole source over an impedance surface and the other is acoustic wave propagation in a duct with a finite impedance wall. Both single-frequency and broadband-frequency simulations are performed within the framework of linearized Euler equations. A high-order dispersion-relation-preserving finite-difference method and a low-dissipation, low-dispersion Runge–Kutta method are used for spatial discretization and time integration, respectively. The results show excellent agreement with the analytical/experimental results at various frequencies. The method accurately predicts both the amplitude and the phase of acoustic pressure and ensures the well-posedness of the broadband time-domain impedance boundary condition. © *2009 Acoustical Society of America.* [DOI: 10.1121/1.2999339]

PACS number(s): 43.28.Js, 43.28.En, 43.20.Rz [GCL] Pages: 664–675

I. INTRODUCTION

The acoustic impedance condition in computational aeroacoustic (CAA) applications, such as the calculation of sound propagation and absorption through an engine inlet duct and the reflection of acoustic waves in outdoor propagation, is an important issue.[1] Until now, several analytical attempts have been made to solve problems of acoustic wave reflection above an impedance surface. Analytical solutions and asymptotic formulas are useful and efficient if one is interested in a single observer point in an acoustic field. Li and White[2] derived an analytical expression of acoustic waves by a harmonic point source above an impedance surface. Di and Gilbert[3] recently represented the total acoustic field due to a point source above a complex impedance plane as a sum of the free space field and an image-source field, and obtained an image integral, which is relatively simple and rapidly convergent compared to the usual Sommerfeld integral. In more realistic and complicated broadband-frequency problems, however, it can be considerably difficult, if not impossible, to find analytical or approximate expressions. Because experimental approaches can be laborious and expensive, time-domain numerical approaches provide an attractive alternative for analyzing the effect of an impedance surface on the propagation of acoustic waves generated by broadband sources, such as a high-speed impulsive source.

Recently, several attempts[4–14] have been made to implement the impedance boundary conditions in the context of the time-domain methodology in CAA. Davis[4] considered acoustic waves in an open-ended pipe and solved the relevant one-dimensional equations using a fourth-order compact difference scheme with low-dispersion error and no amplitude dissipation error. He obtained the impedance boundary condition at the open end of the pipe by the inverse Fourier transform of the standard frequency-dependent impedance for transients with predominant low-frequency content. Bottledooren[5] proposed a finite-difference time-domain method for the simulation of the acoustic field on an analytically generated quasi-Cartesian grid and a simple expression for the impedance boundary condition relating pressure to the corresponding normal velocity where the normal impedance is given. The advantage of the method for the curved impedance boundary is demonstrated. Tam and Auriault[6] developed time-domain single-frequency and broadband impedance boundary conditions for the three-parameter impedance model of the Helmholtz resonator type. Zheng and Zhuang[7,8] verified and validated their broadband time-domain impedance boundary condition in semi-infinite two- and three-dimensional ducts with acoustically treated walls. Their impedance model, however, is a simple resonant type that cannot be extended to the general impedance problem. A general impedance condition was proposed by Long and co-workers[9,10] based on the z-transform. They pointed out that although the impedance model in rational form provides "quite accurate resistance and reactance representations of the experimental impedance data used in this paper, these representations did not meet the stability and causality criteria" as it does not ensure that the poles of the impedance lie within the unit circle in the z-domain, and that the region of convergence lies outside the outermost pole. Furthermore,

[a]Electronic mail: jbin@scs.fsu.edu
[b]Electronic mail: myh@cespr.fsu.edu
[c]Electronic mail: solee@snu.ac.kr

for accuracy, it may require a high degree of the rational function, which in turn requires high-order derivatives of the pressure and the velocity resulting in increased computational time. Fung and Ju[11–13] discussed some issues concerning the modeling and implementation of the time-domain impedance boundary condition. They showed that the reflection process corresponding to a typical impedance model is a convolution of the incident waves and the reflection impulse (which is the inverse Fourier transform of the reflection coefficient). It is pointed out that a direct inversion of impedance into time-domain boundary operators generally leads to an unstable system, whereas the inversion of the corresponding reflection coefficient results in stable, easily implementable boundary operators for time-domain prediction of wave reflection. They validated their models with the available analytical and experimental results. Although this approach is convenient to approximate an impedance curve and to treat the impedance condition numerically, high-order polynomial expansions for the reflection coefficient may lead to severe over- or underpredictions beyond the limited frequency region of interest. Furthermore, it is difficult to represent the resonance phenomena in the impedance curve using this approach. The impedance modeling technique of Wilson *et al.*[14] cast the convolution integrals of their relaxation impedance model in a form amenable to numerical implementation, and it has been demonstrated on two-dimensional calculations of outdoor sound propagation involving hills, barriers, and ground surfaces with various material properties. This approach is both computation and memory intensive since convolution integrals are involved.

The objective of this paper is to develop a robust, accurate, and practical time-domain impedance boundary condition for acoustic simulation with broadband frequencies. To validate this condition, two kinds of numerical simulations are performed: one is acoustic propagation due to point sources over an impedance surface in an open field and the other is noise propagation in a duct with a finite impedance wall. Examples of a typical grass ground impedance and a wool-felt ground impedance are used to illustrate the practicality and effectiveness of the impedance model for the first case.[15] Both single-frequency and broadband-frequency calculations are performed. The second set of examples is for acoustic propagation in a two-dimensional duct with a finite ceramic tubular liner (CT73).[10,16] The numerical solutions are compared with the analytical/experimental results in both cases.

The paper is organized as follows. Section II provides brief mathematical preliminaries, and succinct derivation of the impedance boundary condition followed by a brief description of the discretization scheme. Section III describes the validation problems with their governing equations, boundary conditions, and discretization scheme. Numerical results are presented in Sec. IV.

II. BROADBAND IMPEDANCE BOUNDARY CONDITION

A. Mathematical preliminaries

The characteristics of acoustic impedance are measured and usually described in the frequency domain. Myers[17] and Ingard[18] derived a general acoustic impedance boundary condition assuming that an acoustically treated wall makes deformations in response to an incident acoustic field from the fluid and ignoring a possible hydrodynamic mode.[19] These deformations are assumed to be small perturbations compared to a stationary mean surface, and the corresponding fluid velocity field is a small perturbation about a mean base flow u_0. The linearized frequency-domain impedance boundary condition with mean flow is expressed as

$$\hat{u}(\omega)\cdot n=(i\omega+u_0\cdot\nabla-n\cdot(n\cdot\nabla u_0))\frac{\hat{p}(\omega)}{i\omega Z(\omega)}. \tag{1}$$

Here $\hat{u}(\omega)$ is the complex amplitude of the velocity perturbation, ω is the angular frequency, n is the normal vector to the wall that points into the wall, $\hat{p}(\omega)$ is the complex amplitude of the pressure perturbation, and $Z(\omega)=R(\omega)+iX(\omega)$ [where $R(\omega)$ and $X(\omega)$ are the frequency-dependent resistance and reactance, respectively] is the acoustic impedance. (All these quantities are nondimensionalized with respect to their corresponding characteristic values, which are defined in Sec. III.) The use of this condition is limited to linear unsteady flow problems. Since the mean flow mainly satisfies $u_0\cdot n=0$ on the wall, this equation can be recast into

$$\hat{u}(\omega)\cdot n=(i\omega+u_0\cdot\nabla+u_0\cdot(n\cdot\nabla n))\frac{\hat{p}(\omega)}{i\omega Z(\omega)}, \tag{2}$$

where $n\cdot\nabla n$ is tangential to the wall surface and vanishes for a flat surface. If $Z(\omega)$ is assumed to be independent of position, we get the following form by multiplying $i\omega Z(\omega)$ by both sides of Eq. (2):

$$i\omega Z(\omega)\hat{u}(\omega)\cdot n=i\omega\hat{p}(\omega)+u_0\cdot\nabla\hat{p}(\omega)+u_0\cdot(n\cdot\nabla n)\hat{p}(\omega). \tag{3}$$

By applying the inverse Fourier transform to Eq. (3) and considering the causality condition, we get the impedance boundary condition in the physical domain as follows:

$$\frac{1}{2\pi}\int_0^t z(t-\tau)\frac{\partial}{\partial\tau}u(\tau)\cdot n\,d\tau=\frac{\partial p}{\partial t}+u_0\cdot\nabla p+u_0\cdot(n\cdot\nabla n)p. \tag{4}$$

If there is no mean flow, the impedance condition of Eq. (3) can be simply expressed by

$$\hat{p}(\omega)=Z(\omega)(\hat{u}(\omega)\cdot n), \tag{5}$$

$$p(t)=\frac{1}{2\pi}\int_0^t z(t-\tau)u(\tau)\cdot n\,d\tau, \tag{6}$$

where $p(t)$ and $u(t)$ denote the inverse Fourier transforms of $\hat{p}(\omega)$ and $\hat{u}(\omega)$ at the impedance wall, respectively. The impedance $z(t)$ is given by

$$z(t)=\int_{-\infty}^{\infty}Z(\omega)e^{i\omega t}d\omega. \tag{7}$$

The evaluation of the convolution integrals in Eqs. (4) and (6) is computationally expensive and may become prohibitively expensive especially for multidimensional CAA prob-

lems. We propose a relatively efficient and robust broadband time-domain impedance model, which circumvents the convolution integral problem.

B. Derivation of the broadband time-domain impedance boundary condition

With $\hat{v}(\omega)=\hat{u}(\omega)\cdot n$, Eq. (3) reads

$$i\omega\hat{p}(\omega)+u_0\cdot\nabla\hat{p}(\omega)+u_0\cdot(n\cdot\nabla n)\hat{p}(\omega)=-i\omega Z(\omega)\hat{v}(\omega). \tag{8}$$

The term $u_0\cdot(n\cdot\nabla n)\hat{p}(\omega)$ is usually small, which is the case if the curvature of the wall does not vary significantly, and hence it is usually neglected. In this study, the impedance surface is a plane and it is rightly neglected. Then the acoustic impedance boundary condition in the frequency domain can be expressed as

$$i\omega\hat{p}(\omega)+u_0\cdot\nabla\hat{p}(\omega)=-i\omega Z(\omega)\hat{v}(\omega). \tag{9}$$

To proceed further, we need to model the impedance, $Z(\omega)$.

1. The impedance model

Care must be exercised in modeling the impedance so that it provides the impedance boundary condition in a form that is amenable to an efficient direct numerical simulation of acoustics involving response to broadband frequencies. As the second-order frequency response function (FRF) can act as a low-pass filter or a bandpass filter, we propose to represent the impedance as a linear sum of FRFs (and provide *a posteriori* justification) as follows:

$$Z(\omega)=\sum_{j=1}^{N}\frac{a_0^j(i\omega)+a_1^j}{b_0^j(i\omega)^2+b_1^j(i\omega)+b_2^j}, \tag{10}$$

where N is the number of FRFs and the a's and b's are the constants/parameters that are so determined as to yield the best approximation to the empirical data. These parameters can be determined by common optimization methods, such as a nonlinear least squares fit algorithm or the steepest descent method. In this study, the conjugate gradient method is used to obtain the optimal values of the parameters,[20,21] which yield accurate representations of the well-known two-parameter empirical impedance model[1,15] and of experimental data from NASA.[10,16] The stability analysis in the appendixes shows that the impedance model is stable if all model parameters are real and positive. With N equal to 4, we obtain a good approximation of engineering accuracy for the impedance of the grass ground and the wool-felt ground, respectively (Figs. 4 and 5). Again, the impedance model fits very well with the Langley experimental data of a ceramic tubular liner (CT73) (Fig. 6). Further discussion is deferred to Sec. IV.

After the substitution of $Z(\omega)$ from Eq. (10) in Eq. (9), with some algebra and manipulation, we obtain

$$i\omega\hat{p}(\omega)+u_0\cdot\nabla\hat{p}(\omega)=i\omega\left[\sum_{j}^{N}\hat{p}_j(\omega)\right], \tag{11a}$$

$$\hat{p}_j(\omega)=-\hat{\nu}(\omega)\frac{a_0^j(i\omega)+a_1^j}{b_0^j(i\omega)^2+b_1^j(i\omega)+b_2^j},\quad j=1,\ldots,N, \tag{11b}$$

which are obtained from Eqs. (5) and (10). The inverse Fourier transform of Eq. (11a) yields

$$\frac{\partial p}{\partial t}+u_0\cdot\nabla p=\sum_{j}^{N}\frac{\partial p_j}{\partial t}. \tag{12}$$

To implement this impedance boundary condition, we should obtain the values of pressure, p_j or their derivatives, $\partial p_j/\partial t$. The pressure p_j's are the auxiliary values introduced by the impedance model of Eq. (10) and only depend on the normal velocity perturbation at the impedance surface. Thus, each p_j can be computed separately from the physical values, such as the pressure and normal velocity at the wall. Now, $\hat{p}_j(\omega)$ can be rearranged into the following form after applying the inverse Fourier transform to Eq. (11b):

$$\left(b_0^j\frac{\partial^2 p_j}{\partial t^2}+b_1^j\frac{\partial p_j}{\partial t}+b_2^j p_j\right)=-\left(a_0^j\frac{\partial \nu}{\partial t}+a_1^j\nu\right),\quad j=1,\ldots,N, \tag{13}$$

where v is the normal velocity perturbation on the wall, and p_j is the pressure of the jth subcomponent in Eq. (12).

C. Discretization scheme

Using the second-order finite-difference scheme, Eq. (13) can be discretized as

$$\left(b_0^j\frac{p_j^{(n+1)}-2p_j^{(n)}+p_j^{(n-1)}}{\Delta t^2}+b_1^j\frac{p_j^{(n+1)}-p_j^{(n-1)}}{2\Delta t}+b_2^j p_j^{(n+1)}\right)=-\left(a_0^j\frac{\nu^{(n+1)}-\nu^{(n-1)}}{2\Delta t}+a_1^j\nu^{(n)}\right) \tag{14}$$

for $j=1,\ldots,N$. The solution of Eq. (14) for the acoustic pressure at the $(n+1)$ time step, $p_j^{(n+1)}$, requires the acoustic velocity at the $(n+1)$ time step, $v^{(n+1)}$ [and the acoustic pressure and velocity at the (n) and $(n-1)$ time steps], implying the implicit nature of the impedance condition. The implicit discretization of Eq. (13) may enhance the numerical stability, but results in additional complexity. In order for the impedance boundary condition to be implemented explicitly, the normal momentum equation at the impedance wall is applied. Substituting for $\partial v/\partial t$ from the y-momentum equation in Eq. (21), Eq. (14) becomes

$$\left(b_0^j\frac{p_j^{(n+1)}-2p_j^{(n)}+p_j^{(n-1)}}{\Delta t^2}+b_1^j\frac{p_j^{(n+1)}-p_j^{(n-1)}}{2\Delta t}+b_2^j p_j^{(n+1)}\right)=\left(a_0^j\left(M_x\frac{\partial \nu^{(n)}}{\partial x}+\frac{\partial p^{(n)}}{\partial y}\right)-a_1^j\nu^{(n)}\right) \tag{15}$$

for $j=1,\ldots,N$. All of the values except $p_j^{(n+1)}$ are known, or can be computed from the values in the interior computational domain and on the impedance surface at the previous time step. At time level $(n+1)$, $p_j^{(n+1)}$ can be obtained explicitly from the following equation:

$$\left(\frac{b_0^j}{\Delta t^2}+\frac{b_1^j}{2\Delta t}+b_2^j\right)p_j^{(n+1)}=\frac{2b_0^j}{\Delta t^2}p_j^{(n)}-\left(\frac{b_0^j}{\Delta t^2}-\frac{b_1^j}{2\Delta t}\right)p_j^{(n-1)}+\left(a_0^j\left(M_x\frac{\partial \nu^{(n)}}{\partial x}+\frac{\partial p^{(n)}}{\partial y}\right)-a_1^j\nu^{(n)}\right) \tag{16}$$

for $j=1,\ldots,N$. Using the pressure values, p_j, and substituting them into Eq. (12), we get

$$\frac{p^{(n+1)}-p^{(n-1)}}{2\Delta t}+M_x\frac{\partial p^{(n+1)}}{\partial x}=\mathrm{RHS}\left(=\sum_j^N\frac{p_j^{(n+1)}-p_j^{(n-1)}}{2\Delta t}\right). \tag{17}$$

In this study, the temporal and spatial derivatives of the pressure in the impedance condition are discretized using the second-order central difference scheme

$$Ap_{(k-1,l)}^{(n+1)}+Bp_{(k,l)}^{(n+1)}+Cp_{(k+1,l)}^{(n+1)}=\frac{p_{(k,l)}^{(n-1)}}{2\Delta t}+\mathrm{RHS}, \tag{18}$$

$$A=-\frac{M_x}{2\Delta x},\quad B=\frac{1}{2\Delta t},\quad C=\frac{M_x}{2\Delta x}, \tag{19}$$

where the subscript (k,l) in Eq. (19) is the grid point index in the x- and y-directions, respectively. Specifically, l represents the grid point at the impedance surface in Eq. (18). For simplicity, a uniform mesh is chosen with $\Delta x=\Delta y=\mathrm{const}$. This results in a tridiagonal matrix form. If fourth-order spatial discretization is used in Eq. (17), a pentadiagonal equation matrix system will result. If there is no mean flow in the computational domain ($M_x=0$), the impedance boundary condition, Eq. (12), can be simply expressed as

$$p^{(n+1)}=\sum_j^N p_j^{(n+1)}. \tag{20}$$

To make this impedance boundary condition satisfy the causality condition, acoustic perturbations are assumed to be absent for $t<0$ and all physical values are set to zero for $t<0$ in the numerical simulations. The computed results using the broadband time-domain impedance boundary condition will be compared with the analytical/experimental solutions.

III. VALIDATION PROBLEMS

To validate our time-domain broadband impedance methodology, we choose two example problems: (i) the computation of the sound field above an impedance ground relevant to outdoor sound propagation, and (ii) the computation of the sound field in a duct with mean flow relevant to acoustic fields inside and radiated from both inlet and exhaust of turbofan engines.

A. Governing equations

We assume that the linearized Euler equations govern the acoustic field

$$\frac{\partial U}{\partial t}+A_x\frac{\partial U}{\partial x}+B_y\frac{\partial U}{\partial y}+mSU=mF, \tag{21}$$

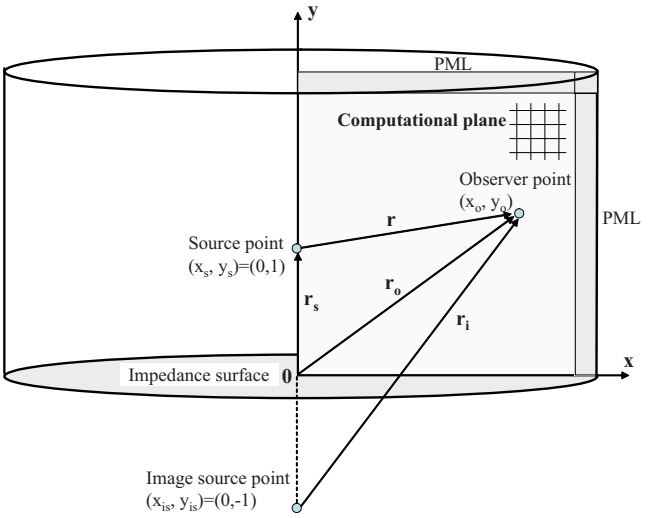

FIG. 1. (Color online) Coordinate system of a point monopole source over an impedance surface.

$$U=\begin{pmatrix}\rho\\ u\\ \nu\\ p\end{pmatrix},\quad A_x=\begin{pmatrix}M_x & 1 & 0 & 0\\ 0 & M_x & 0 & 1\\ 0 & 0 & M_x & 0\\ 0 & 1 & 0 & M_x\end{pmatrix},$$

$$B_y=\begin{pmatrix}M_y & 0 & 1 & 0\\ 0 & M_y & 0 & 0\\ 0 & 0 & M_y & 1\\ 0 & 0 & 1 & M_y\end{pmatrix},\quad S=\frac{1}{x}\begin{pmatrix}0 & 1 & 0 & 0\\ 0 & M_x & 0 & 0\\ 0 & 0 & 0 & 0\\ 0 & 1 & 0 & 0\end{pmatrix}, \tag{22}$$

where (x,y) represent the coordinates, ρ is the density perturbation, u and v are the velocity perturbations in the x- and y-directions, respectively, p is the pressure perturbation, $\mathbf{F}$ is the source vector, and M_x and M_y represent the Mach number in the x- and y-directions, respectively. For two-dimensional problems, $m=0$, and for axisymmetric problems, $m=1$, where (x,y) represent the radial and the axial coordinates, respectively. In this paper, density, velocity, and pressure are nondimensionalized by ρ_∞, c_∞, and $\rho_\infty c_\infty^2$, respectively. Quantities with the subscript ∞ denote the ambient conditions with c_∞ being the speed of sound. The coordinates (x,y) are scaled with respect to an appropriate length, L, which characterizes the problem. The characteristic length in Problem 1 is the height of the monopole source above the impedance surface, and in Problem 2 it is the duct height.

Problem 1: Acoustic wave reflection on an impedance surface (no mean flow). The sound field due to an acoustic monopole source in a homogeneous medium without mean flow above an impedance ground is cylindrically symmetric, in that there is no azimuthal variation. In order to consider three-dimensional acoustic wave propagation, cylindrical coordinates are used, where x is the radial coordinate, y is the axial coordinate, and $y=0$ is the impedance plane. Figure 1 shows the schematic of the coordinate system and the computational domain. The height of the monopole source, H^*, from the impedance plane is the characteristic length of the

problem, with which all lengths are scaled, and thus the acoustic source is located at $(x_s, y_s)=(0,1)$. An image-source point is used to obtain the analytic solution at an observer point.[3]

To simulate the acoustic field, Eq. (21) (with the source vector defined as $\mathbf{F}=[f_m,0,0,f_m]^T$) is solved with the following initial and boundary conditions.

Initial condition: $U=(\rho,u,v,p)^T=0$.

Boundary conditions: At the impedance boundary, $y=0$, the time-domain impedance boundary condition [Eq. (17)] is applied. At the radial open boundary, $x=x_\infty$, and the axial open boundary, $y=y_\infty$, the perfectly matched layer (PML) method[22–25] is applied. Axial symmetry condition is applied at $x=0$.

We consider both single-frequency and broadband-frequency cases.

Case (a): Periodic reflection at a single frequency. A monopole source is introduced to generate an acoustic wave in the computational domain. Following Ju and Fung,[3] we introduce a monopole source equivalent to a point monopole source strength, which is written as

$$f_m(r,t)=\frac{1}{B_w^3\pi^{3/2}}e^{-(r/B_w)^2}e^{(kB_w)^2/4}\sin(\omega t), \tag{23}$$

where $r=|r_s-r_o|$ is the distance between the observer at r_o and the source point at r_s, B_w is the half-width of a Gaussian distribution, and k is the wave number. The half pulse-width relative to the characteristic length $\bar{B}_w=B_w/H^*$ used for a monopole is very small ($\bar{B}_w=0.0375$) to maintain solution smoothness and to ensure equivalence with a point monopole source. The nondimensional coordinates of the monopole source are $(x,y)=(0,1)$, where the coordinates have been scaled with respect to the characteristic length represented by the height, H^*, of the source above the impedance surface. Here H^* is assumed to be equal to $2\lambda^*$, where $\lambda^*=c_\infty/f$. We chose the frequency $f=3$ kHz as the human ear is most sensitive around 2–5 kHz, and many acoustic simulations and applications to sound reduction have used the frequency range around it.

Case (b): Excess attenuation at broadband frequencies. For broadband-frequency simulations, we introduce monopole sources containing several frequencies of interest, and obtain the response over an impedance wall. For this, the monopole source term is defined as

$$f_m(x,y,t)=0.01\sum_{m=1}^{45}e^{-\ln 2(((x-x_s)^2+(y-y_s)^2)/B^2)}\times\cos\left[\left(\omega_0+2\pi(m-1)\frac{100}{c_\infty}\right)t+2(m-1)\pi/45\right], \tag{24}$$

$$x_s=0,\quad y_s=1.0,\quad B=\frac{2\pi}{2[\omega_0+2\pi(m-1)\times 100/c_\infty]}, \tag{25}$$

where $\omega_0=2\pi f_0$ with $f_0=500/c_\infty$ and $c_\infty=340$ m/s, which corresponds to 500 Hz.

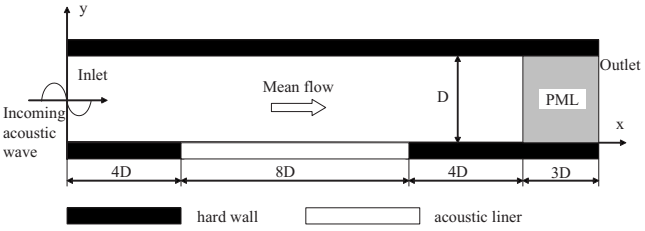

FIG. 2. The schematic of the flow-impedance duct.

Problem 2: Sound propagation in a duct with a finite impedance wall (with mean flow). We consider sound propagation in a semi-infinite two-dimensional duct with a finite impedance wall and unidirectional mean flow ($M_x=0.1$, $M_y=0.0$). The characteristic length is naturally the height of the duct, D. Figure 2 is the schematic of the computational domain. Equation (21) is solved with the following initial and boundary conditions.

Initial condition: $U=(\rho,u,v,p)^T=0$.

Inflow boundary condition: Assuming a uniform mean flow in the x-direction, the acoustic disturbances would satisfy the following radiation boundary condition at inflow ($x=0$):

$$\left\{\frac{\partial}{\partial t}-(1-M_x)\frac{\partial}{\partial x}\right\}\begin{pmatrix}\rho\\u\\v\\p\end{pmatrix}=-2\frac{\partial}{\partial x}\begin{pmatrix}\rho_d\\u_d\\v_d\\p_d\end{pmatrix}. \tag{26}$$

The downstream propagating wave at the inflow region $[\rho_d\ u_d\ v_d\ p_d]^T$ can be written as

$$\begin{pmatrix}\rho_d\\u_d\\v_d\\p_d\end{pmatrix}=A(t)\begin{pmatrix}1\\1\\0\\1\end{pmatrix}\sin\left\{\omega\left(\frac{x}{1+M_x}-t\right)+\varphi\right\}, \tag{27a}$$

$$A(t)=\text{Amp}\times\exp\left[-\ln 2\frac{(y-1)^2}{\{3\times\Delta y\times(1+t)\}^2}\right], \tag{27b}$$

where $A(t)$ and φ denote the amplitude and the phase of the incoming acoustic waves, respectively. The constant Amp is set to $\sqrt{2}p_{\text{ref}}10^{\text{SPL}/20}/\rho_\infty c_\infty^2$ with $p_{\text{ref}}=2.0\times10^{-5}$ Pa and $\varphi=0$. The implementation of the time-domain impedance boundary condition requires physical information from the previous time step. To avoid the transient effect of incoming waves on the response of an impedance surface, a Gaussian distributed incoming wave amplitude, as expressed in Eq. (27b), is introduced, which precludes abrupt jumps of physical values in the initial stage near the impedance wall.

Outflow boundary condition. At the damping layer, ($16\leqslant x\leqslant 19$), the two-dimensional PML method[22–25] is used to damp out the waves to prevent their reflection back into the domain of computation.

At the upper rigid wall ($y=1$), the normal velocity is set to zero. At the bottom impedance boundary ($y=0$), the time-domain impedance boundary condition [Eq. (17)] is imposed.

B. Numerical algorithm

In this work, the seven-point stencil dispersion-relation-preserving (DRP) scheme is used for spatial discretization.[26] A low-dissipation, low-dispersion Runge–Kutta method is used for time integration.[27]

1. Numerical damping

The DRP scheme is a central difference scheme with fourth-order accuracy with zero intrinsic dissipation. In order to eliminate spurious short waves and to improve numerical stability, two kinds of damping terms are used in this computation. The first kind is artificial selective damping proposed by Tam and Webb,[26] which is added to the discretized finite-difference equations, as shown in Eq. (29). An inverse mesh Reynolds number $R_\Delta^{-1}=\nu_a/(a_\infty\Delta)$, where ν_a and Δ are the artificial kinematic viscosity and mesh size, respectively, is prescribed over the whole computational domain to damp out the spurious waves.

$$U_{k,l}^{(n+1)} = U_{k,l}^{(n)} + \Delta t \sum_{j=0}^{3} b_j K_{k,l}^{(n-j)}, \tag{28}$$

$$K_{k,l}^{(n)} = -\frac{1}{\Delta x} A_x \sum_{j=-3}^{3} a_j U_{k+j,l}^{(n)} - \frac{1}{\Delta y} B_y \sum_{j=-3}^{3} a_j U_{k,l+j}^{(n)} - mSU_{k,l}^{(n)} + \bar{D}_{k,l}(U) + D_{k,l}(U), \tag{29}$$

$$\bar{D}_{k,l}(U) = (\bar{D}_x)_{k,l} + (\bar{D}_y)_{k,l} = -\frac{L}{\Delta x R_\Delta} \sum_{j=-3}^{3} d_j (U_{k+j,l}^{(n)} + U_{k,l+j}^{(n)}). \tag{30}$$

Near the wall a reduced number of points are used for damping, i.e., $j=-2,\ldots,2$ at $l=3$ and $j=-1,\ldots,1$ at $l=2$ in $(\bar{D}_y)_{k,l}$. The coefficients and the details can be found in Ref. 26.

On the impedance surface, there exists a mismatch of velocity and pressure because of their relationship in the acoustic impedance condition. Therefore, the amplitudes and the phases of the incoming waves to the impedance wall will be changed after the reflection from the surface. Furthermore, due to the use of the second- or fourth-order finite-difference discretization for the impedance condition in Eqs. (14) and (17), all of the time impedance information cannot be included in this discretization. To remove unphysical surface waves, which may be generated in this process, and to obtain the stable solution of the acoustic reflection from the surface, the following dissipation is used in the interior domain. Fourth-order dissipation is used with the second-order computations of the impedance condition, and sixth-order dissipation is used with the fourth-order computations

$$D_{k,l}^{(4)}(U) = -\kappa^{(4)}(\delta_x^{(4)} + \delta_y^{(4)})U, \quad D_{k,l}^{(6)}(U) = \kappa^{(6)}(\delta_x^{(6)} + \delta_y^{(6)})U, \tag{31a}$$

$$\delta_x^{(4)} U = \sum_{i=-2}^{2} w_i U_{k+i,l} \quad \text{with } w_i = [1\ \ -4\ \ 6\ \ -4\ \ 1] \quad \text{for } i=-2,\ldots,2, \tag{31b}$$

$$\delta_x^{(6)} U = \sum_{i=-3}^{3} w_i U_{k+i,l} \quad \text{with } w_i = [1\ \ -6\ \ 15\ \ -20\ \ 15\ \ -6\ \ 1] \quad \text{for } i=-3,\ldots,3. \tag{31c}$$

Typical values of the constants $\kappa^{(4)}$ and $\kappa^{(6)}$ are $1/128$ and $1/512$, respectively. The y-direction operators are defined in a similar manner. Dissipation is set to zero if values beyond a boundary are needed in the computation. It was found from the numerical simulation that the use of two kinds of damping can effectively eliminate the small amplitude three-point oscillations without affecting the accuracy of the physical solution and was critical in obtaining stable numerical solutions.

TABLE I. The parameter values used in the computation (Ref. 15.)

	Effective flow resistivity (σ_e) (kPa s m^{-2})	Effective rate of change of porosity (α_e) (m^{-1})
Grass-covered ground	100	20
Wool-felt material	38	15

IV. RESULTS AND DISCUSSION

A. The impedance model

Problem 1: Acoustic wave reflection over an impedance surface. In the following calculations, an empirical two-parameter impedance model[15] is used for the impedance data, where the normalized specific impedance Z of the ground is given by

$$Z = 0.436(1-i)\left(\frac{\sigma_e}{f}\right)^{0.5} - 19.48i\frac{\alpha_e}{f}, \tag{32}$$

where f is the frequency, and σ_e and α_e are the effective flow resistivity and the effective rate of change of porosity with depth, respectively. This model has often been used to fit excess attenuation data, especially that measured outdoors.[15] In this study, two types of parameter values are used for the validation of the impedance boundary condition. The parameters are given in Table I.

The objective is to determine the impedance function $Z(\omega)$ in Eq. (10), which is the best approximation to the empirical curve [Eq. (32)]. To that end, we choose frequencies ω_l, $l=1,2,3,\ldots,N_{\text{total}}$ from the frequency range of interest, and for each frequency we construct a FRF whose peak equals the impedance value at that frequency. Specifically, a second-order bandpass filter has the peak frequency and bandwidth, respectively, given by $\omega_0^2=b_2/b_0$ and $\beta=b_1/b_0$. The initial values of a's are arbitrarily assumed to be unity. Figure 3 shows the schematic of the initial FRFs and the experimental impedance curve. With this initial guess of impedance,

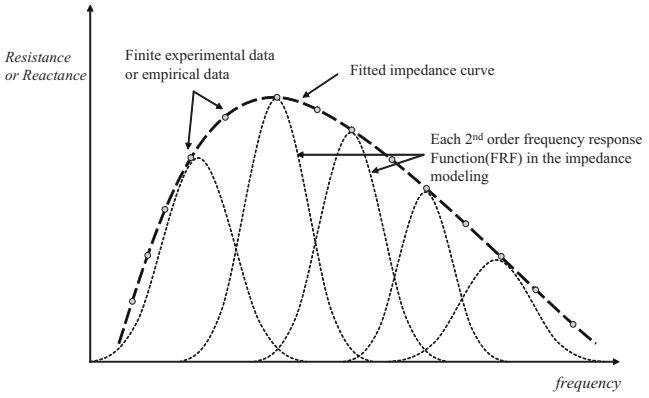

FIG. 3. The schematic of a modeled impedance function.

$$Z_l = Z(\omega_l) = \sum_{j=1}^{N} \frac{a_0^j (i\omega_l) + a_1^j}{b_0^j (i\omega_l)^2 + b_1^j (i\omega_l) + b_2^j}, \tag{33}$$

we start the minimization process of the objective function $I=\Sigma_{l=1}^{N_{\text{total}}}(Z_l-Z_l)^2$ (where Z_l are the empirical or experimental data) to obtain the optimal values of the parameters a's and b's. In the present case, we initially chose four uniformly spaced frequencies (specifically, $\omega_l=2,4,6,8$ kHz) in the frequency range of interest for both the grass and wool-felt grounds. With these as peak frequencies, initial FRFs are constructed to form the initial Z_l, and start the optimization process. Initial guess is important to ensure convergence of the optimization process to the right critical point. The convergence tolerance on the parameter value is on the order of 10^{-6}. The optimal parameter values are given in Appendix A.

Figures 4 and 5 show the comparison between the two-parameter impedance model[15] and the fitted impedance model used in this study for a grass ground and a wool-felt ground. There is an excellent agreement between the empirical curve and the fitted model. In these figures, individual

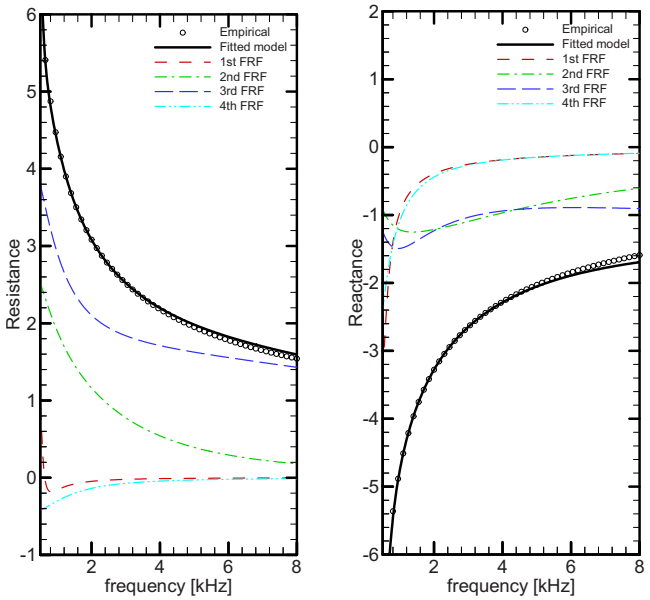

FIG. 4. (Color online) Fitted impedance model (solid line) and empirical model (circles): surface impedance of the typical grass ground. The individual FRFs are shown for comparison of their impedance content.

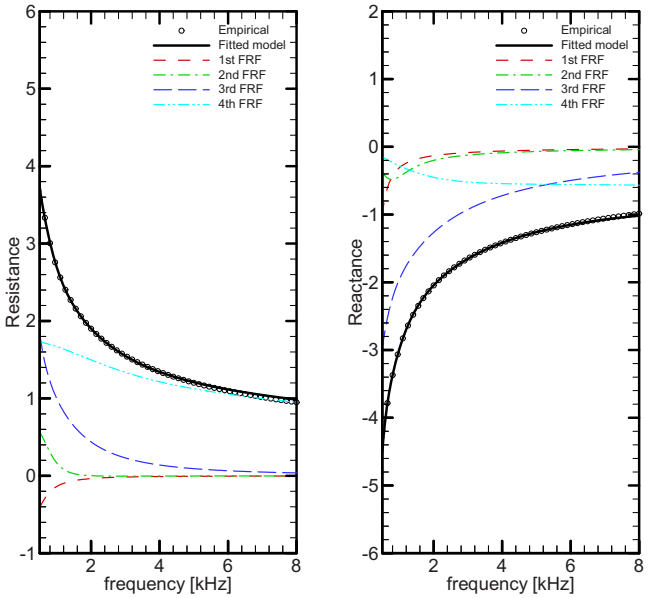

FIG. 5. (Color online) Fitted impedance model (solid line) and empirical model (circles): surface impedance of the typical wool-felt material. The individual FRFs are included to show their relative impedance content.

FRFs are also plotted to show that most FRFs contain the contributions of all the frequencies of interest (from 500 to 8 kHz) in both the resistance and the reactance, owing to broadband characteristic of the impedance surface.

Problem 2: Acoustic wave propagation in a duct with a finite acoustic liner. The input data used to extract the impedance of the test specimen were obtained from measurements using a flow-impedance tube at the NASA Langley Flow-Impedance Test Laboratory.[9,10,16] To fit our impedance model to the experimental data, we proceeded as in the case of Problem 1 except that we set the peaks of the FRFs at $\omega_l=1000$, 1500, 2000, 2500, and 3000 Hz. The optimal values of the model parameters are given in Appendix A. Figure 6 shows the comparison between the experimental values and the fitted model. Excellent agreement is observed. The

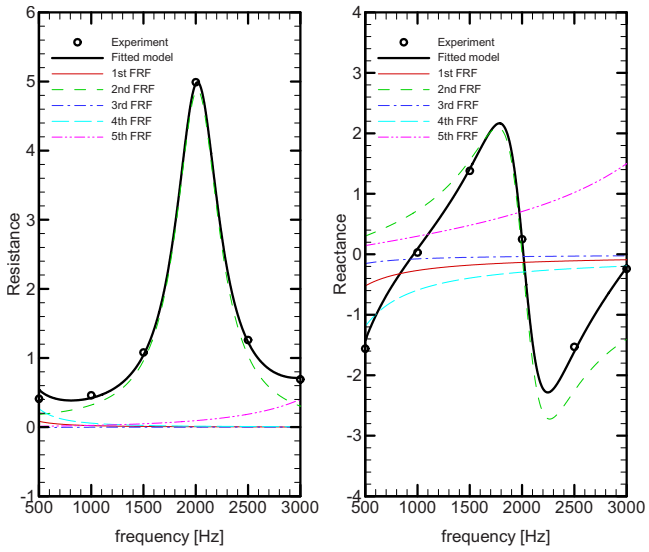

FIG. 6. (Color online) Fitted impedance model (solid line) and experimental data (circles) for resistance and reactance of a ceramic tubular liner (CT73).

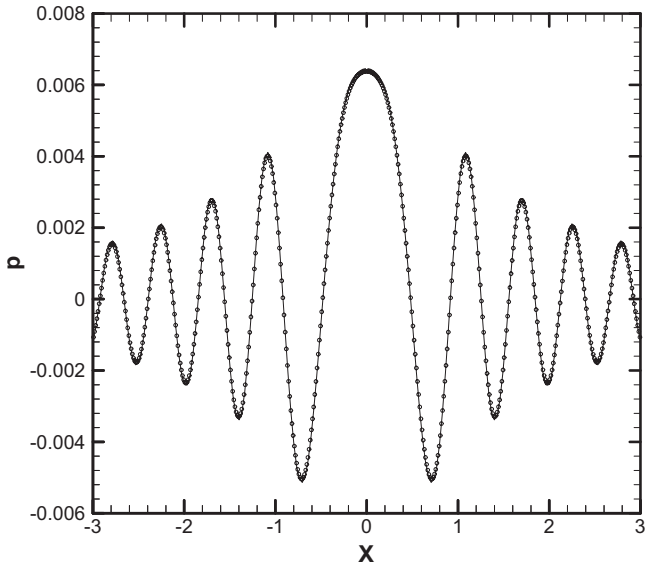

FIG. 7. Comparison of harmonic pressure distribution computed in time domain (symbols) with analytical solution (solid line) on the impedance surface ($y=0$) at $t=50$ T at $f=3$ kHz over a grass ground ($Z=2.52-2.65i$).

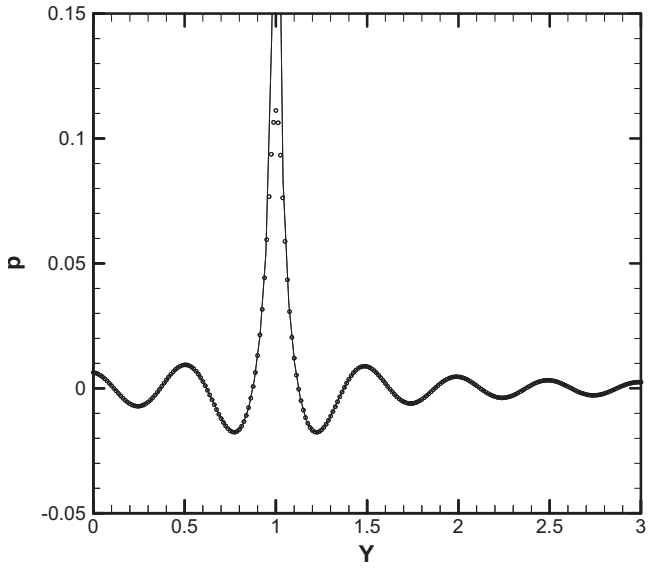

FIG. 8. Comparison of harmonic pressure distribution computed in the time domain (symbols) with analytical solution (solid line) along the line perpendicular to the impedance surface, i.e., axisymmetric line ($x=0$) at $t=50$ T at $f=3$ kHz over a grass ground.

impedance characteristic shows the resonance phenomenon in the impedance curve. The contribution of the second FRF term among the five FRFs that make up the impedance curve is dominant when compared with the other terms. Improvement in the impedance model can be obtained by increasing the number of FRFs, but we obtain satisfactory results using four or five FRFs in each problem.

B. Numerical validation

Case (a): Periodic reflection at a single frequency (Problem 1). In order to validate the impedance boundary condition, the numerical simulation of sound reflection over an impedance wall at a single frequency is performed. In this computation, the grid spacing and dimensions are $\Delta x=\Delta y=1/80$ and $D_x\times D_y=3\times 3$ in the x- and y-directions, respectively. Computations are performed using a nondimensional time step of $\Delta t=\mathrm{CFL}\Delta x$ where the Courant–Friedrich–Lewy (CFL) number has the value of 0.05.

Figures 7 and 8 show comparisons of the harmonic pressure distribution computed in the time domain with the analytical solution on the impedance surface ($y=0$) and along the line perpendicular to the impedance surface ($x=0$) at $t=50$ T at $f=3$ kHz over a grass ground ($Z=2.52-2.65i$). Figures 9 and 10 compare the analytical solution with the numerical solution using the present impedance boundary condition for an impedance value of wool felt at $f=3$ kHz ($Z=1.55-1.65i$). These figures show excellent agreement between the analytical and numerical solutions.

Case (b): Excess attenuation at broadband frequencies (Problem 1). To show that the impedance boundary condition works well in broadband problems, excess attenuation at broadband frequencies is performed and compared with an analytical solution in this section. The numerical simulation was performed on a 461×241 equally spaced grid in both the x- and y-directions ($\Delta x=\Delta y=1.13\times 10^{-2}$) with a CFL number of 0.05. In this computation, monopole sources containing 45 frequencies are considered, as is obvious from Eq. (24). Time signals stored at the observer points are used to compute the sound pressure level (SPL) (in decibels) for comparing the excess attenuation. The time data required to compute the SPL are stored after the sound field reaches the periodic state. Figure 11 compares the prediction of excess attenuation, which is defined as the total sound field relative to the direct field, for a monopole. The source and observer height are 1.0 m and 0.5 m, respectively, and the separation range along the x-direction for the comparison is 1.0 m. Figure 11 shows the comparison of excess attenuation between the computed result and the analytical solution for a grass ground and for a wool-felt ground. A fast Fourier transform

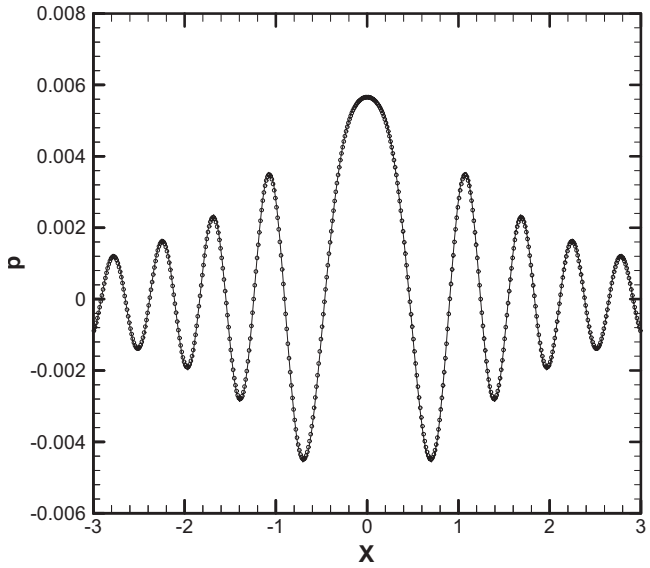

FIG. 9. Comparison of harmonic pressure distribution computed in the time domain (symbols) with analytical solution (solid line) on the impedance surface ($y=0$) at $t=50$ T at $f=3$ kHz over a wool-felt ground ($Z=1.55-1.65i$).

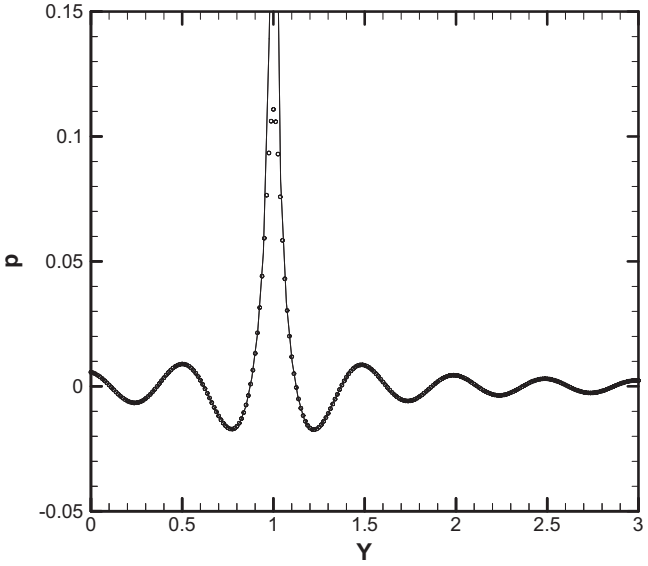

FIG. 10. Comparison of harmonic pressure distribution computed in the time domain (symbols) with analytical solution (solid line) along the line perpendicular to the impedance surface, i.e., axisymmetric line (x=0) at t =50 T at f=3 kHz over a wool-felt ground.

is used to obtain the SPL for each individual frequency from the time accurate signals. To obtain the SPL of the direct field, additional numerical computations without an impedance wall were performed. It can be seen from these figures that there is a little difference between the predicted and the analytical excess attenuation spectra for a monopole source. The agreement between the calculations and the analytical solution gives us confidence that it is possible to get accurate broadband numerical solutions using the broadband time-domain impedance boundary condition developed in this paper.

1. Absorption in an acoustic liner with mean flow (Problem 2)

The numerical simulations were performed on a 571 $\times$31 equally spaced grid in both the x- and y-directions ($\Delta x=\Delta y$) with a CFL number of 0.02. An acoustic wave of SPL=130 dB is introduced at the inflow boundary. The acoustic pressure signals required to compute the SPL along the upper wall are collected after the transients leave the computational domain and the field becomes periodic. Numerical computations were performed at six different frequencies from 0.5 to 3.0 kHz at 0.5 kHz increments. Fourth-order spatial discretization is employed in both the x- and y-directions for the governing equations and second-order discretization is used for the broadband impedance boundary condition, as mentioned in Eq. (15).

Figure 12 shows the comparison of the upper wall SPL results for the current calculations with the measured data. The symbols in these figures indicate the experimental data. The agreement between the measurements and the current results is excellent. In Fig. 12, it is shown that sound absorption in an acoustic liner is a function of frequency and that the large absorption occurs at 1.0 kHz and the small absorption occurs at 2.0 kHz.

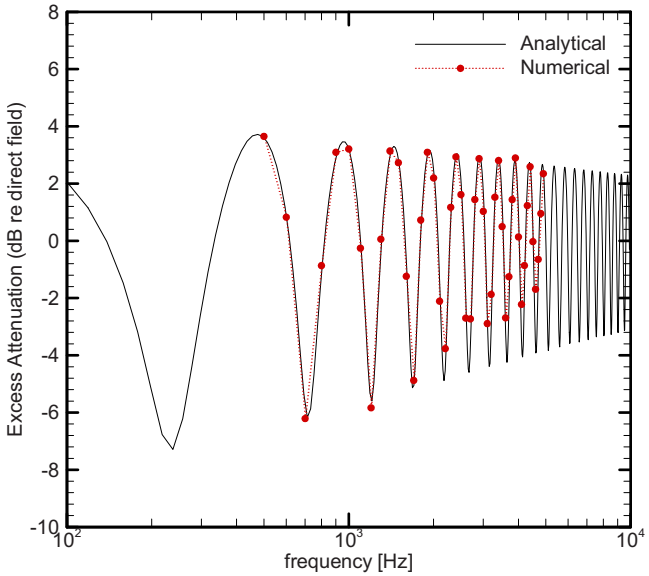

(a) Grass ground

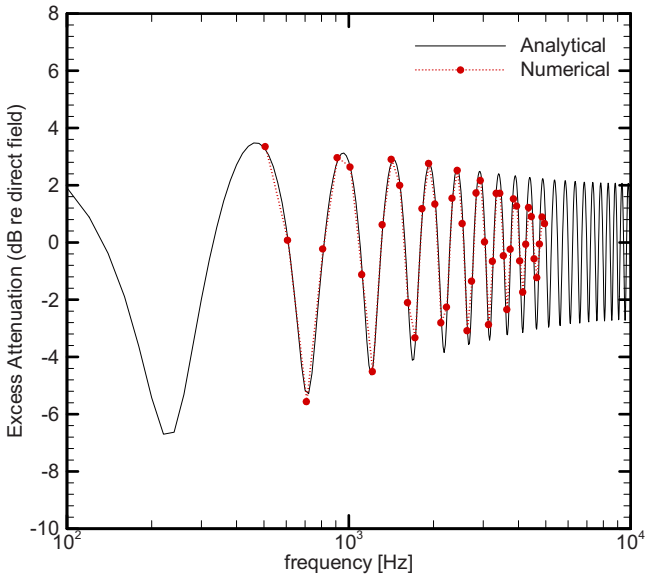

(b) Wool ground

FIG. 11. (Color online) Comparison of excess attenuation of sound due to a monopole between computed result (symbols) and analytical solution (solid line). The source-receiver geometry is y_s=1.0, y_o=0.5, and range equals 1.0. (a) Grass ground; (b) wool ground.

V. SUMMARY AND CONCLUSIONS

In this paper, a broadband time-domain impedance boundary condition has been developed and validated. The frequency-domain impedance condition was represented as a linear sum of second-order frequency response functions, assuming that the impedance is independent of the location on the surface. This allowed the construction of a bandpass filter and a low-pass filter type response function as the approximation to the expensive convolution integral in the conventional time-domain impedance condition. This frequency response function utilizes the past pressure and velocity outputs, and the present acoustic pressure inputs recursively. Two-dimensional numerical experiments reveal that there is

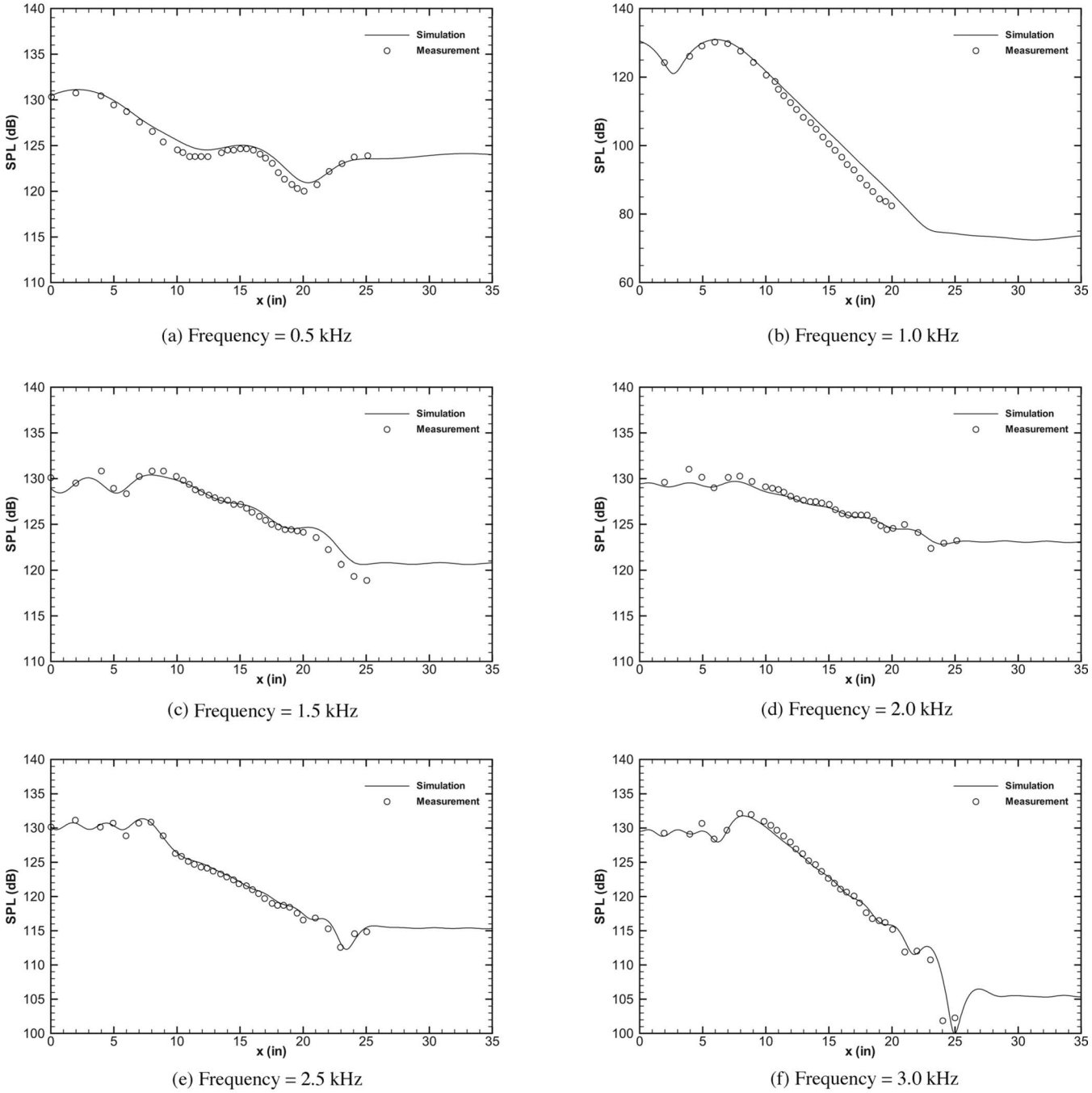

FIG. 12. Upper wall SPLs given by the single-frequency simulations. $M=0.1$: (a) $f=0.5$ kHz, (b) $f=1.0$ kHz, (c) $f=1.5$ kHz, (d) $f=2.0$ kHz, (e) $f=2.5$ kHz, and (f) $f=3.0$ kHz.

good agreement between the numerical results and analytical/experimental solutions and indicate that the present method is capable of accurately simulating the physical broadband phenomena over acoustically treated surfaces.

It stands to reason that the frequency-domain methods in situations where they are readily implementable may outperform the present time-domain impedance boundary condition or any time-domain approach. But then the present method is intended for real-world problems that may not be amenable to frequency-domain methods or current time-domain approaches. Having demonstrated the validity, robustness, and practicality of the method, its relative performance vis-à-vis other time-domain methods remains to be established in the context of acoustic simulations involving broadband frequencies, such as impulsive noise, turbulence noise, etc. It is but proper to mention that it may be difficult if not impossible to apply the current methodology to such problems. It will be the topic of future work.

ACKNOWLEDGMENT

J.B. gratefully acknowledges the financial assistance from the Office of the Provost.

APPENDIX A: BROADBAND-FREQUENCY IMPEDANCE FUNCTION

The curves shown in Figs. 4–6 were obtained by applying a conjugate gradient method[20,21] to the frequency-domain impedance function given by Eq. (10). A total of four FRFs were used in both cases of a grass ground and a wool-felt ground. A total of five FRFs were employed for the case of an acoustic liner. The parameters a_0^j to b_2^j of this equation were found to be

$$Z(\omega) = \sum_{j=1}^{4} \frac{a_0^j(i\omega) + a_1^j}{b_0^j(i\omega)^2 + b_1^j(i\omega) + b_2^j},$$

$$\omega = 2\pi f \quad \text{where } f \text{ is in Kilohertz.} \tag{A1}$$

1. The coefficients for the grass ground

$a_0^1 = 0.704\,173\,53/2\pi$, $a_1^1 = 0.387\,007\,09$,

$b_0^1 = 0.957\,422\,22/(2\pi)^2$, $b_1^1 = 0.274\,703\,90/2\pi$, $b_2^1 = 0.183\,504\,06$,

$a_0^2 = 0.771\,817\,02/2\pi$, $a_1^2 = 1.193\,269\,66$,

$b_0^2 = 0.144\,220\,47/(2\pi)^2$, $b_1^2 = 0.574\,349\,11/2\pi$, $b_2^2 = 0.404\,762\,86$,

$a_0^3 = 0.579\,089\,01/2\pi$, $a_1^3 = 1.311\,837\,80$,

$b_0^3 = 1.724\,860\,51 \times 10^{-2}/(2\pi)^2$, $b_1^3 = 0.340\,938\,39/2\pi$, $b_2^3 = 0.293\,515\,78$,

$a_0^4 = 0.500\,873\,21/2\pi$, $a_1^4 = 1.162\,788\,45$,

$b_0^4 = 0.706\,389\,34/(2\pi)^2$, $b_1^4 = 0.877\,132\,11/2\pi$, $b_2^4 = 1.393\,761\,61 \times 10^{-3}$.

2. The coefficients for the wool-felt material ground

$a_0^1 = 0.840\,338\,25/2\pi$, $a_1^1 = 0.730\,370\,99$,

$b_0^1 = 3.400\,127\,98/(2\pi)^2$, $b_1^1 = 0.965\,755\,94/2\pi$, $b_2^1 = 0.234\,801\,97$,

$a_0^2 = 1.692\,764\,18/2\pi$, $a_1^2 = 2.358\,337\,75$,

$b_0^2 = 5.064\,137\,35/(2\pi)^2$, $b_1^2 = 5.960\,787\,85/2\pi$, $b_2^2 = 3.448\,883\,64$,

$a_0^3 = 2.978\,427\,78/2\pi$, $a_1^3 = 2.118\,550\,71$,

$b_0^3 = 0.972\,494\,18/(2\pi)^2$, $b_1^3 = 1.476\,833\,16/2\pi$, $b_2^3 = 0.200\,666\,12$,

$a_0^4 = 0.506\,580\,59/2\pi$, $a_1^4 = 2.442\,884\,62$,

$b_0^4 = 2.142\,249\,30 \times 10^{-2}/(2\pi)^2$, $b_1^4 = 0.534\,803\,50/2\pi$, $b_2^4 = 1.395\,599\,61$.

3. The coefficients for the ceramic tubular liner (CT73)

$a_0^1 = 15.142\,262\,85$, $a_1^1 = 2.201\,562\,75$,

$b_0^1 = 8.958\,174\,74$, $b_1^1 = 5.807\,517\,92$, $b_2^1 = 0.472\,299\,49$,

$a_0^2 = 1.429\,013\,44$, $a_1^2 = 2.352\,884\,52$,

$b_0^2 = 9.351\,699\,97 \times 10^{-2}$, $b_1^2 = 0.294\,350\,28$, $b_2^2 = 15.251\,511\,51$,

$a_0^3 = 2.509\,711\,50$, $a_1^3 = 1.319\,491\,80$,

$b_0^3 = 5.325\,179\,34$, $b_1^3 = 1.907\,520\,80$, $b_2^3 = 1.004\,487\,05$,

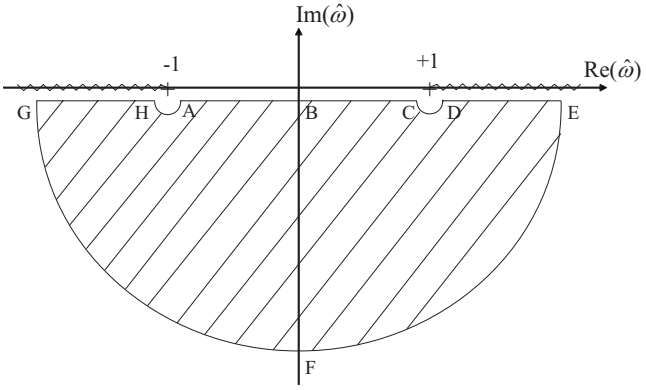

FIG. 13. Area of $\hat{\omega}$ plane.

$a_0^4 = 2.781\,151\,08$, $a_1^4 = 3.844\,384\,27$,

$b_0^4 = 0.753\,678\,58$, $b_1^4 = 1.474\,136\,38$, $b_2^4 = 1.155\,048\,05$,

$a_0^5 = 2.628\,979\,68 \times 10^{-2}$, $a_1^5 = 5.682\,839\,61 \times 10^{-3}$,

$b_0^5 = 7.627\,031\,04 \times 10^{-4}$, $b_1^5 = 4.203\,121\,55 \times 10^{-3}$, $b_2^5 = 0.580\,376\,55$.

APPENDIX B: THE WELL-POSEDNESS OF THE BROADBAND FREQUENCIES FOR IMPEDANCE SURFACES

Assuming the impedance surface is located in the x-z plane and applying the Fourier–Laplace transform to the governing equations, which are the linearized Euler equations, it can be found that the solution satisfies the outgoing wave condition at $y \to \infty$ as follows: Consider the separable solutions

$$\begin{bmatrix} p(x,y,z,t) \\ u(x,y,z,t) \\ v(x,y,z,t) \\ w(x,y,z,t) \end{bmatrix} = \begin{bmatrix} \tilde{p}(y) \\ \tilde{u}(y) \\ \tilde{v}(y) \\ \tilde{w}(y) \end{bmatrix} \times e^{i(\Omega t - \alpha x - \beta z)}. \tag{B1}$$

By substituting these equations into the governing equations, the corresponding solutions can be obtained in the following form:

$$\begin{bmatrix} \tilde{p}(y) \\ \tilde{u}(y) \\ \tilde{v}(y) \\ \tilde{w}(y) \end{bmatrix} = A \begin{bmatrix} 1 \\ \alpha/\Omega \\ -(\hat{\omega}^2 - 1)^{1/2}/\hat{\omega} \\ \beta/\Omega \end{bmatrix} \times e^{ik(\hat{\omega}^2 - 1)^{1/2} y}, \tag{B2}$$

where $\hat{\omega} = \Omega/k$, $k = (\alpha^2 + \beta^2)^{1/2}$, and $A = \text{const}$. The branch cuts of the function $(\hat{\omega}^2 - 1)^{1/2}$ are taken to be $0 \leqslant \arg(\hat{\omega}^2 - 1)^{1/2} \leqslant \pi$, as shown in Fig. 13.

The Fourier–Laplace transforms of the impedance condition are expressed as

$$\tilde{p} = -\frac{a_0 + a_1/(i\Omega)}{b_0(i\Omega) + b_1 + b_2/(i\Omega)} \tilde{v}. \tag{B3}$$

Substitution of Eq. (B2) into Eq. (B3) leads to the following dispersion relation:

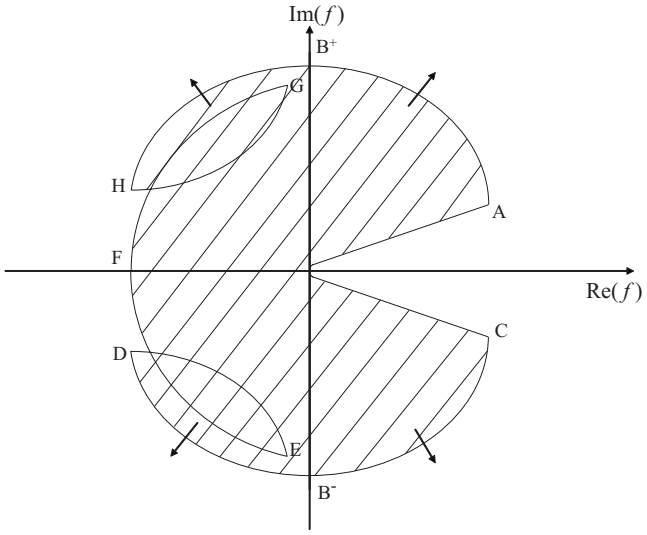

FIG. 14. Map of the lower half of $\hat{\omega}$ in the $f(\hat{\omega})$ plane.

$$\left(kb_0(i\hat{\omega}) + b_1 + \frac{b_2/k}{i\hat{\omega}}\right)\left(\frac{\hat{\omega}}{(\hat{\omega}^2-1)^{1/2}}\right) + \frac{a_1}{k\hat{\omega}}i = a_0. \quad \text{(B4)}$$

In this equation all of the coefficients of a's and b's are real, positive numbers. This boundary treatment is well posed if this equation has no solutions in the lower half of the $\hat{\omega}$ plane depicted in Fig. 13. Let the left-hand side of this equation be expressed by $f(\hat{\omega})$.

$$f(\hat{\omega}) = \left(kb_0(i\hat{\omega}) + b_1 + \frac{b_2/k}{i\hat{\omega}}\right)\left(\frac{\hat{\omega}}{(\hat{\omega}^2-1)^{1/2}}\right) + \frac{a_1}{k\hat{\omega}}i. \quad \text{(B5)}$$

Figure 14 shows the map of the lower half $\hat{\omega}$ plane in the f plane. For the case of $a_0 > 0$, there is no value of $\hat{\omega}$ in the lower half of the $\hat{\omega}$ plane that can satisfy the dispersion relation of Eq. (B4), since the right-hand side of Eq. (B4) is real and positive. So it can be proven that there is no stability problem in the case where all of the coefficient values are real and positive.

[1]A. D. Pierce, *Acoustics—An Introduction to Its Physical Principles and Applications* (Acoustical Society of America, New York, 1989).
[2]Y. L. Li and M. J. White, "Near-field computation for sound propagation above ground-using complex image theory," J. Acoust. Soc. Am. **99**, 755–760 (1996).
[3]X. Di and K. E. Gilbert, "An exact laplace transform formulation for a point source above a ground surface," J. Acoust. Soc. Am. **93**, 714–720 (1993).
[4]S. Davis, "Low-dispersion finite difference methods for acoustic waves in a pipe," J. Acoust. Soc. Am. **90**, 2775–2781 (1991).
[5]D. Botteldooren, "Acoustical finite-difference time-domain simulation in a quasi-cartesian grid," J. Acoust. Soc. Am. **95**, 2313–2319 (1994).
[6]C. K. W. Tam and L. Auriault, "Time-domain impedance boundary conditions for computational aeroacoustics," AIAA J. **34**, 917–923 (1996).
[7]S. Zheng and M. Zhuang, "Three-dimensional benchmark problem for broadband time-domain impedance boundary conditions," AIAA J. **42**, 405–407 (2004).
[8]S. Zheng and M. Zhuang, "Verification and validation of time-domain impedance boundary condition in lined duct," AIAA J. **43**, 306–313 (2005).
[9]Y. Özyörük, L. N. Long, and M. G. Jones, "Time-domain numerical simulation of a flow-impedance tube," J. Comput. Phys. **146**, 29–57 (1998).
[10]Y. Özyörük and L. N. Long, "A time-domain implementation of surface acoustic impedance condition with and without flow," J. Comput. Phys. **5**, 277–296 (1997).
[11]K.-Y. Fung and H. Ju, "Broadband time-domain impedance models," AIAA J. **39**, 1449–1454 (2001).
[12]H. Ju and K.-Y. Fung, "Time-domain impedance boundary conditions with mean flow effects," AIAA J. **39**, 1683–1690 (2001).
[13]H. Ju and K.-Y. Fung, "Time-domain simulation of acoustic sources over an impedance plane," J. Comput. Acoust. **10**, 311–329 (2002).
[14]D. K. Wilson, V. E. Ostashev, S. L. Collier, N. P. Symons, D. F. Aldridge, and D. H. Marlin, "Time-domain calculations of sound interactions with outdoor ground surfaces," Appl. Acoust. **68**, 175–200 (2007).
[15]K. Attenborough, "Ground parameter information for propagation modeling," J. Acoust. Soc. Am. **92**, 418–427 (1992).
[16]T. L. Parrott, W. R. Watson, and M. G. Jones, "Experimental validation of a two-dimensional shear-flow model for determining acoustic impedance," Technical Report No. TP-2679 (NASA, Washington, DC, 1987).
[17]M. K. Myers, "On the acoustic boundary condition in the presence of flow," J. Sound Vib. **71**, 429–434 (1980).
[18]U. Ingard, "Influence of fluid motion past a plane boundary on sound reflection, absorption, and transmission," J. Acoust. Soc. Am. **31**, 1035–1036 (1959).
[19]S. W. Rienstra, "Impedance models in time domain including the extended helmholtz resonator model," 12th AIAA/CEAS Aeroacoustics Conference, Cambridge, MA, 8–10 May 2006.
[20]W. H. Press, B. P. Flannery, S. A. Teukolsky, and W. T. Vetterling, *Numerical Recipes in FORTRAN 77: The Art of Scientific Computing*, 2nd ed. (Cambridge University Press, Cambridge, 1992).
[21]E. K. P. Chong and S. H. Zak, *An Introduction to Optimization*, 2nd ed. (Wiley, New York, 2001).
[22]H. E. Hayder, F. Q. Hu, and M. Y. Hussaini, "Towards perfectly absorbing boundary conditions for the Euler equations," AIAA J. **37**, 3135–3144 (1999).
[23]F. Q. Hu, "On absorbing boundary conditions for the linearized Euler equations by a perfectly matched layer," J. Comput. Phys. **129**, 201–219 (1996).
[24]F. Q. Hu, "A stable, perfectly matched layer for linearized Euler equations in unsplit physical variables," J. Comput. Phys. **173**, 455–480 (2001).
[25]S. Abarbanel, D. Stanescu, and M. Y. Hussaini, "Unsplit variables perfectly matched layers for the shallow water equations with Coriolis forces," Comput. Geosci. **7**, 275–294 (2003).
[26]C. K. W. Tam and J. C. Webb, "Dispersion-relation-preserving finite difference schemes for computational aeroacoustics," J. Comput. Phys. **107**, 262–281 (1993).
[27]F. Q. Hu, M. Y. Hussaini, and J. L. Manthey, "Low-dissipation and low-dispersion Runge–Kutta schemes for computational acoustics," J. Comput. Phys. **124**, 177–191 (1996).